Numerical Heart Transfer, Part A: Applications, Volume 70, Issue 8, 2016, pp. 815-830
DOI:10.1080/10407782.2016.1214494

Numerical solution of three-dimensional rectangular submerged jets with evidence of the undisturbed region of flow

M. Angelino[a], A. Boghi[b], F. Gori[c,*]

[a] Loughborough University, Aeronautical and Automotive Engineering, Stewart Miller Building, Loughborough LE11 3TU, UK

[b] Cranfield University, School of Engineering, Environment and Agrifood, Whittle Building, Bld 52, Cranfield, MK43 0AL, UK

[c*]Corresponding author, University of Rome "Tor Vergata", Department of Industrial Engineering, Via del Politecnico 1, 00133 Rome, Italy.

Abstract

The evolution of turbulent rectangular submerged free jets has been investigated numerically with a two-dimensional approach, [1], by using the Large Eddy Simulations (LES) at several Reynolds numbers. The average numerical results confirmed the presence of the undisturbed region of flow, URF, located between the slot exit and the beginning of the potential core region, PCR, previously observed experimentally at the University of Rome "Tor Vergata". The two-dimensional study, [1], carried out under the conditions previously investigated in the literature, showed that the URF has a self-similar behavior, and proposed a new law for the evolution of the momentum. The present paper extends the Large Eddy Simulations (LES) to three-dimensional rectangular submerged free jets, showing that the self-similar behavior of URF is present also in the three-dimensional numerical simulations, as well as in the PCR and in the fully developed region, FDR.

1. Introduction

The interpretation of the evolution of turbulent rectangular submerged free jets, investigated in the last decades, can be summarized by the interaction of the jet with the stagnant fluid just after the slot exit, [2], defining two regions of flow: the Potential Core Region (PCR) and the Fully Developed Region (FDR). The flow in the PCR and FDR has been studied theoretically by Tollmien [3] and Görtler [4], who found self-similar velocity profiles in those regions of flow. The proposed equations describing their evolutions have been confirmed experimentally for the PCR [5-9], and the FDR, [10-13].

The experiments carried out at the University of Rome "Tor Vergata" by Gori and coworkers investigated the flow evolution of a rectangular jet of air, with Hot Wire Anemometer (HWA) and shadowgraph visualizations, [14-15], Hot Film Anemometer (HFA) and shadowgraph visualizations, [16-18], and Particle Image Velocimetry (PIV), [19-20]. The presence of a third region of flow, which has been called undisturbed region of flow, URF, has been observed in the average visualizations and measurements, [19], and located between the slot exit and the beginning of the potential core region, PCR. The average experiments established that its length diminishes with the increasing Reynolds number. Further experiments with the Particle Image Velocimetry (PIV) on the instant flow evolution, [20], have shown that the URF can

Published by Taylor and Francis. This is the Author Accepted Manuscript issued with: Creative Commons Attribution Non-Commercial License (CC:BY:NC 4.0). The final published version (version of record) is available online at DOI:10.1080/10407782.2016.1214494. Please refer to any applicable publisher terms of use.

be further divided into two new types of flow, the negligible disturbances flow (NDF) and the small disturbances flow (SDF). In the NDF the jet height remains almost constant, as well as the velocity and the turbulence profiles, while, in the SDF, the jet height evidences small contractions or expansions, but without the formation of vortices.

Looking back to previous experiments of the literature it has been possible to recognize that a region of flow, which can be considered an Undisturbed Region of Flow (URF), was already been observed experimentally for certain inlet conditions [21-23]. In other experimental works, [24-27], Direct Numerical Simulations (DNS), [28-29], and Large Eddy Simulations (LES), [30], the evidence of an URF can be found, but none of these papers discussed about it.

The URF has not been investigated numerically so far, except in [31], where preliminary numerical solutions, obtained with the RANS modeling, were compared with the experimental shadowgraph visualizations at Re=25,000 and 60,000. The previous study of the same authors, [1], has been carried out, with a series of Large Eddy Simulations (LES) at several Reynolds numbers, to verify that the URF occurs in the conditions previously given by the literature [2] in a two-dimensional, 2D, case.

The numerical analysis can give further information, besides the experiments, which can contribute to a better understanding of the phenomenon of heat transfer upon a cylinder, due to jet flow [32-35]. This problem has been shown to depend on several variables, as the presence of multiple cylinders in a row [36-37], fins [38-42], level of turbulence in the jet [43-44] and slot to cylinder diameter ratios [45-46].

This work presents the results of three-dimensional (3D) Large Eddy Simulations (LES) of a rectangular free jet, at several Reynolds numbers, which extends the two-dimensional approach, [1], in order to show that also in the three-dimensional case it is possible to define self-similar relations for the URF, and to asses that the theoretical model is valid also in presence of a turbulent profile on the slot exit.

2. Numerical Method

2.1 Governing Equations

In the LES approach the governing equations are derived by filtering the Navier-Stokes equations. This is particularly easy in the case of an incompressible fluid. The filtered variables are indicated with the superscript $\tilde{}$. Applying the filtering operation to the mass and momentum equations the following equations are obtained

$$\frac{\partial \tilde{u}_i}{\partial x_i} = 0 \tag{1}$$

$$\frac{\partial \tilde{u}_i}{\partial t} + \frac{\partial}{\partial x_j}\left(\tilde{u}_i \tilde{u}_j + \tilde{p}\delta_{ij} - \frac{2}{\mathrm{Re}} \tilde{S}_{ij} \right) = \frac{\partial \tau_{ij}^{sgs}}{\partial x_j} \tag{2}$$

where u_i is the velocity vector, p the static pressure, δ_{ij} the identity tensor. The Reynolds number Re is defined as

$$\mathrm{Re} = \frac{U_{in} D_h}{\nu} \tag{3}$$

where U_{in} is the inlet velocity, D_h the hydraulic diameter, defined as four times the ratio between the slot area and its perimeter, and ν the fluid kinematic viscosity. The shear rate tensor, S_{ij}, is defined as

$$\tilde{S}_{ij} = \frac{1}{2}\left(\frac{\partial \tilde{u}_i}{\partial x_j} + \frac{\partial \tilde{u}_j}{\partial x_i} \right) - \frac{1}{3}\frac{\partial \tilde{u}_k}{\partial x_k}\delta_{ij} \tag{4}$$

The sub-grid stress tensor τ_{ij}^{sgs} is

$$\tau_{ij}^{sgs} = 2\nu_{sgs}\tilde{S}_{ij} - \frac{2}{3}k_{sgs}\delta_{ij} \tag{5}$$

the sub-grid viscosity

$$\nu_{sgs} = C_S \Delta^2 \tilde{S} \tag{6}$$

the sub-grid kinetic energy

$$k_{sgs} = C_I \Delta^2 \tilde{S}^2 \tag{7}$$

the filtered shear rate

$$\tilde{S} = \sqrt{2\tilde{S}_{ij}\tilde{S}_{ij}} \tag{8}$$

the filter width

$$\Delta = \sqrt{\Delta_m \Delta_m} \tag{9}$$

with Δ_k the box filter width in the m-th direction. The dynamic Smagorinsky model is employed in this study.

2.2. Computational Details

The simulations are realized with the pisoFoam finite-volume solver of the open-source code OpenFOAM, which solves the Navier-Stokes transient incompressible equations via the PISO algorithm. The 3D grid is generated with blockMesh, the OpenFOAM utility for mesh generation, at all the Reynolds numbers. The geometry is made of a rectangular box, 2 diameter long in the transverse direction (*z*), 3 diameters in the vertical (*y*) and 6.5 diameters in the axial direction(*x*). The grid is uniform in the *z* direction,

and stretched in the *x* and *y* directions near the slot exit, although the minimum and maximum grid stencils are of the same order of magnitude. In the *z* direction the stencil is $\Delta z = 0.0197$ hydraulic diameters, while in the *x* and *y* directions they are $\Delta x, \Delta y = 0.0074 \div 0.0294$ hydraulic diameters. The grid is made of $442 \times 262 \times 102$ points. The explicit time integration scheme is of the second order backwards, and of the second order central for the spatial derivatives. The time step in each simulation satisfies the condition CFL < 0.5. The filter chosen in OpenFOAM is the "simple" one, which is the surface integral of the face interpolated of the field. The filter amplitude is the cubic root of the cell volume.

A wall is present above and below the slot, with a thickness of 0.176 hydraulic diameters, as in the experiments [19-20]. Everywhere else, i.e. in the *x* and *y* direction, a free boundary is present. The total pressure is imposed on the outlet boundaries, as well as the velocity boundary condition, which changes according to its direction. If the fluid flows out of the domain a zero gradient condition is imposed for the velocity, otherwise the velocity is obtained from the patch-face normal component of the internal-cell value. This boundary condition in OpenFOAM is known as "pressureInletOutletVelocity". A periodic boundary condition is imposed in the span-wise direction.

The simulations are carried out for 30 flow times, being the "flow time" the ratio between the domain length and the axial velocity on the slot exit. The steady state is assumed to be reached after 10 flow times, while the following 20 flow times are employed to average the instantaneous variables and to obtain the mean turbulent properties.

A top-hat velocity profile is assumed on the slot exit, in analogy with the experiments of [2], with the addition of some disturbances in order to trigger the turbulence in the 3D simulations. A small perturbation of 1 % in the amplitude of the velocity profile is enough to produce a 3D flow. The technique proposed by Lee et al. [47] is adopted, with the advantage of injecting the disturbance in the low and intermediate wave number ranges, where it cannot be immediately damped. Let decompose the discrete perturbation velocity field u_k in Fourier series

$$u_k = \frac{1}{N}\sum_{n=0}^{N-1} U_n e^{2\pi i k n/N} \tag{10}$$

where U_n are the complex Fourier modes, which can be written as $U_n = |U_n| e^{i\varphi_n}$. According to the Parseval theorem

$$\sum_{n=0}^{N-1} E_n = \sum_{m=0}^{N-1} |u_m|^2 = \frac{1}{N}\sum_{n=0}^{N-1} |U_n|^2 \tag{11}$$

In order to generate a perturbation, which is able to reproduce the turbulent energy spectrum, it is assumed that $|U_n| = \sqrt{NE_n}$ and φ_n is a random function of n. The turbulent spectrum is given by

$$E(k) \propto k^4 e^{-2\left(\frac{k}{k_0}\right)^2} \tag{12}$$

with

$$k = \sqrt{k_x^2 + k_y^2 + k_z^2} \tag{13}$$

The inlet perturbation field is assumed to act in the three directions.

The simulations have been performed on the Blue Gene/Q system "Fermi" of the Italian supercomputing center CINECA, having requested around 200,000 CPU hours for all the simulations.

3. Results and discussion.

The results are presented for the four Reynolds numbers and all the variables are expressed in non-dimensional form.

3.1 Instant variables

The iso-surfaces of the instant vorticity magnitude are reported in Fig. 1 at the four Reynolds numbers investigated. Despite the presence of a 1% perturbation in the amplitude of the velocity profile, the free shear layer shows an initial undisturbed behavior. A plausible explanation is that on the slot exit, i.e. at the interface between jet and stagnant air, the velocity gradient is so steep that the turbulent stresses are negligible compared to the viscous ones. The Kelvin-Helmholtz instability appears in the free shear layer at different times and positions according to the Reynolds number. Higher is the Reynolds number, earlier the roller vortex structures form and closer they are to the slot exit. This is in agreement with the linear theory of the Kelvin-Helmholtz instability [48], which prescribes that the wave number of the resonant harmonic is proportional to the ratio of the frequency to the mean velocity, so that a low wave number perturbation is enough to trigger the instabilities at high Reynolds number flows. Also, the vortices structure appears to be bigger at smaller Reynolds numbers.

The roller vortex structures develop symmetrically and travel downstream at the speed of the convection velocity. The z component of the vorticity vector has opposite signs above and below the centerline, which means that the vortices above the centerline roll in the anti-clockwise direction while the vortices below the centerline roll in the clockwise direction. This cannot be seen in Fig.1 because it shows the iso-surfaces of the vorticity magnitude to clarify the jet shape. At a certain distance downstream the beginning of the Kelvin-Helmholtz instability, the roller vortices eventually pair to form a bigger roller structure and the merging of the shear layers, which triggers the asymmetry in the flow.

It is possible to consider the formation of the first Kelvin-Helmholtz instability around the beginning of the PCR, and the beginning of the vortex pairing around its end. In the PCR the resonant sub-harmonic is weak but, as the roller structures travel and pair, it becomes strong enough to activate the asymmetric modes,

which trigger the evolution of the coherent structures. In the PCR, three symmetric couples of counter-rotating vortices can be identified for all the Reynolds numbers shown.

From time to time, different couples of vortices pair to form larger ones, but this phenomenon stops downstream, where the FDR begins. At the beginning of the FDR the vortices break, by virtue of the vortex-stretching, in very small structures which form a turbulent wake. This is the main difference with the numerical results of the two-dimensional case, [1], where this region is not present, but the large eddies occupy the entire domain, forming an asymmetric pattern. The comparison of the present results with the two-dimensional case, [1], confirm that also in presence of a 1% perturbation in the amplitude of the velocity profile it is present a Negligible Disturbance Flow (NDF), immediately after the slot exit, where the jet height remains almost constant, followed by the Small Disturbance Flow (SDF), where the jet height evidences small contractions or expansions but without the formation of vortices, as observed experimentally in [20]. The sum of the length of NDF and SDF is about the same of the Undisturbed Region of Flow (URF), which has been defined for the average variables. The length of NDF and SDF, or URF, decreases with the increase of the Reynolds number, being quite consistent at Re=5000, a little smaller at 10,000, and quite small at Re=20,000 and 40,000.

Figure 1. Instant vorticity iso-surfaces colored by instant velocity magnitude: (a) Re = 5000; (b) Re = 10,000; (c) Re = 20,000; (d) Re = 40,000.

Figure 2 presents the instant isobaric surfaces, shown by different colors, where the blue is indicating the low pressure zones, as well as the instant velocity, which is shown by vectors. The jet undergoes a series of pressure fluctuations across its section, i.e. in the transverse direction, and downstream, i.e. in the streamwise direction. The velocity vectors present a series of accelerations and decelerations in the streamwise direction, especially on the centerline.

The NDF and SDF are clearly visible after the slot exit, as the region where the velocity vectors are almost one-directional and constant. The pressure changes on the two borders of the jet produce symmetric variations of the cross section and correspond to symmetric vortices. The jet section decreases in correspondence to the vortices, and increases between the different vortex pairs, due to the conservations of mass, which implies an increase in the velocity where the section reduces. The Bernoulli equation justifies a pressure increase where the velocity decrease.

Figure 2a, for Re = 5000, shows that the first three concentric isobars along the shear layer present a slight pressure decrease around x=1.9, corresponding to a slight contraction of the cross section, shown also in Fig. 1a. The two following isobars, around x=2.4, on the contrary, present an increase, which can be considered responsible for the expulsion of the fluid from the core of the jet. The formation of the first vortex pair, around x=3.4, is generated because the fluid, after the expulsion, is slowed down by the external small velocity of the stagnant fluid. Around x=5 is present a strong contraction of the cross section, after which the end of the potential core is expected.

Figure 2b presents the results for Re = 10,000. The pattern presents some similarities with Re=5,000, Fig. 2a, except for the length of the NDF and SDF, which are shorter, and the first vortex pair which appears earlier, around x =1.5. The vortices appear almost symmetrical along the jet axis with an alternate pattern, and regions of low and high pressure are visible. The number of vortex pairs is higher compared to the previous case, and two big spots of high pressure are clearly visible around x = 3.5. The velocity vectors at the boundary layer roll backwards because of the pressure gradient.

Figure 2c reports the results for Re = 20,000. The patterns appear somewhat different from the previous two cases, with the presence of several low pressure regions of short extent, which are present between the slot exit and x = 1.3. Downstream this point irregular spots of high pressure are visible. Similar results are shown in Fig. 2d for Re = 40,000.

Figure 2. Instant isobaric surfaces and velocity vectors: (a) Re = 5000; (b) Re = 10,000; (c) Re = 20,000; (d) Re = 40,000.

From the numerical results shown in Figs. 1-2, it is clear that, despite the presence of the 1 % disturbance on the velocity profile at the slot exit, a region of flow free of vortices is present, as in [1], where the inlet profile was flat without turbulence. The instantaneous fields are variable and cannot be employed to identify the average length of the regions of flow. Therefore, the evolution of some mean variables is investigated in order to understand the average effect of the turbulence on the flow.

3.2 Average variables

Figure 3a presents the evolution of the non-dimensional average turbulent kinetic energy, *k*, for Re = 5000. The turbulent kinetic energy is almost null between the slot exit and $x = 1.5$, confirming that, despite the perturbation introduced on the velocity profile at the slot exit, the turbulence develops only at a certain distance downstream, or, in other words, the region is free of turbulence and can be identified with the URF.

Turbulence originates from two points, one above and the other below the centerline, i.e. on the boundary layers between the submerged jet and the stagnant air. Moving downstream from this two points, the turbulent kinetic energy diffuses linearly up to a position where the profiles in the upper and lower parts blend together along the centerline. The region between the two point sources and the connection of the upper and lower profiles has a shape similar to the potential core region, PCR.

Figure 3b shows the turbulent kinetic energy for Re = 10,000, which is negligible close to the slot exit and starts to develop around $x = 1$. Figure 3c shows the *k* contours at Re = 20,000. The beginning of the turbulent kinetic energy is located around $x = 0.1$ and the diffusion in the vertical direction is smaller than in the previous two cases. For Re = 40,000, Fig. 3d, the *k* profile is similar to Re = 20,000, except the source points, which are closer to the slot exit, and the diffusion in the vertical direction, which is even more limited.

Figure 3. Turbulent kinetic energy contours: (a) Re = 5000; (b) Re = 10,000; (c) Re = 20,000; (d) Re = 40,000.

Figure 4 shows the maps of the *x*-*y* component of the Reynolds stress tensor, $\overline{u'v'}$, at the four Reynolds numbers investigated. The stress tensor is reported as positive in the upper part of the domain, and negative in the lower part.

Figure 4a, at Re=5000, shows that, despite the presence of a 1% perturbation on the velocity profile at the slot exit, the Reynolds stresses are negligible up to about x = 1.5, which is equal to the position where turbulent kinetic energy start developing, Fig. 2a. At this axial position there are two points from which the turbulent shear stress originates and spreads downstream. The contours show approximately a linear expansion in the transverse direction, up to a downstream point where the shear stresses in the upper and lower parts of the domain merge. This pattern reminds of the potential core region, although this cannot be establish without inspecting the velocity profile.

Figure 4b, Re = 10,000, shows a pattern of $\overline{u'v'}$ similar to that at Re = 5000, also if the turbulent shear stress starts closer to the slot exit, in agreement to the vorticity and turbulent kinetic energy results, showing a shorter length of the URF. The linear expansion of the turbulent stresses is visible as well, which terminates earlier, and, the upper and lower parts meet at a certain distance.

Figure 4c shows the pattern of $\overline{u'v'}$ at Re = 20,000. The sources of the shear stress are now very close to the slot exit and the area of linear expansion is longer, compared to the previous two cases, terminating earlier, where the positive and the negative stresses meet. Similar considerations can be done for Fig. 4d, where the results for Re = 40,000 are shown. The differences with Re = 20,000 are minors.

Figure 4. $\overline{u'v'}$ *contours: (a) Re = 5000; (b) Re = 10,000; (c) Re = 20,000; (d) Re = 40,000.*

From the two average turbulent variables, i.e. k and $\overline{u'v'}$, it is possible to distinguish two different behaviors in the near-field region, already analyzed in [1], plus a third one in the far-field, which was not captured in the 2D simulations of [1] because of the lack of vortex stretching.

The analysis of the mean axial velocity profile, done in [1], showed the shape of the "isotach" curves in the URF and PCR. The same conclusions can be drawn from the present 3D results, which are not reported here because similar to [1]. The isotachs in the fully developed region, FDR, which could not be captured in the 2D study [1], are reported in the following sections.

3.3 Self-similar solutions in the URF.

The analysis of the variables in the URF suggests that the dependence on the span-wise direction can be neglected. Therefore, despite the presence of a 1% perturbation on the velocity profile at the slot exit, the flow can be considered 2D in the URF, and, in analogy with [1], the following relation can be obtained from the analysis of the isotach

$$\eta = \eta_0 + \sqrt{\mathrm{Re}}\frac{(y-h)}{\sqrt{x}} \tag{14}$$

where *h* is the non-dimensional half-slot vertical coordinate, equal to 0.25.

The analysis of the continuity and momentum equations shows that the jet flow in the URF can be described by the following ordinary differential equation

$$\frac{d^3 f}{d\eta^3} + \frac{1}{2} f \frac{d^2 f}{d\eta^2} = 0 \tag{15}$$

where the axial and vertical velocities can be derived from $f(\eta)$ as

$$u(\eta) = \frac{df}{d\eta} \tag{16}$$

$$v(x,\eta) = -\frac{1}{2}\frac{1}{\sqrt{\mathrm{Re}}}\frac{1}{\sqrt{x}}\left(f - (\eta - \eta_0)\frac{df}{d\eta} \right) \tag{17}$$

The vertical velocity on the centerline is assumed zero, which can be expressed by the following approximate condition

$$\lim_{\eta \to -\infty} f(\eta) = \eta - \eta_0 \tag{18}$$

The third order ordinary differential equation can be solved by splitting it in two systems of three first order differential equations and by imposing the continuity of *f*, $df/d\eta$, and $d^2 f/d\eta^2$, at $\eta = \eta_0$. A numerical code in Matlab is used to solve Eq. (15) through the routine "ode45", which solves the systems of non-linear ordinary differential equations with the Runge-Kutta method of fourth order.

The results confirm the findings of [1], with $\eta_0 = -0.5288$, $f(\eta_0) = -0.3384$, $df/d\eta\big|_{\eta_0} = 0.6914$, and $d^2 f/d\eta^2\big|_{\eta_0} = -0.191$.

Figure 5 compares the numerical axial velocities, obtained from the LES simulations, with the self-similar theoretical values, obtained from the solution of Eq. (15), at the four Reynolds numbers investigated. The numerical results are expressed in function of the self-similarity variable, $\eta - \eta_0$, and are reported at several axial coordinates in order to show that the hypothesis of self-similarity is confirmed. The velocity profile is a monotonically decreasing function, with the maximum at the center of the jet, becoming null in the stagnant air. The results show a very good agreement for the two smaller Reynolds numbers, Re=5000 and Re=10,000. The agreement is fair at Re=20,000 and less good on the axis at the highest Reynolds number, Re=40,000, which can be due to the 1% perturbation imposed on the velocity profile at the slot exit, because the flow is more prone to turbulent transition.

Figure 5. Axial velocity in URF: numerical (points) and present theory of self-similarity (black line): (a) Re = 5000; (b) Re = 10,000; (c) Re = 20,000; (d) Re = 40,000.

3.4 Self-similar solutions in the PCR.

The present numerical results, obtained from the LES approach, are now compared with the theories of Tollmien [3] and Görtler [4], developed for the PCR. Tollmien [3] proposed the following self-similar variable

$$\zeta = \frac{1}{\sqrt[3]{2c^2}} \frac{\left(y - h_0\right)}{\left(x - x_0\right)} \tag{19}$$

which, by imposing a turbulent viscosity proportional to the square of the axial distance and the shear rate, leads to the following ordinary differential equation

$$\frac{d^3 f}{d\zeta^3} + f = 0 \tag{20}$$

Görtler [4] proposed the following self-similar variable

$$\xi = \frac{a}{e} \frac{\left(y - h_0\right)}{\left(x - x_0\right)} \tag{21}$$

which, by imposing a turbulent viscosity proportional to the axial distance, leads to

$$\frac{d^3 f}{d\xi^3} + f \frac{d^2 f}{d\xi^2} = 0 \tag{22}$$

The velocities are related to the function *f* by the following equations

$$U = \frac{a}{\sqrt[3]{2c^2}} \frac{df}{d\zeta} = \frac{a^2}{e} \frac{df}{d\xi} \tag{23}$$

$$V = -a\left(f\left(\zeta\right) - \zeta \frac{df}{d\zeta} \right) = -a\left(f\left(\xi\right) - \xi \frac{df}{d\xi} \right) \tag{24}$$

The span-wise velocity in the Tollmien [3] and Görtler [4] theories is negligible. The coefficients *e* and *c* are non-dimensional parameters directly proportional to the turbulent viscosity, found respectively in [3] and [4]. The coefficient *a*, which appears in both Eq. (23) and (24) is assumed equal to 0.13, while the experimental values span between 0.09, in [19] as well as in [2], and 0.12. From Eq. (24) it follows that the value of the constant a can be deduced from the vertical velocity profile. Equations (20) and (22) are solved providing the boundary conditions imposed in [3] and [4]. The constants can be chosen in such a way that the variables ξ and ζ coincide.

The axial velocity profiles obtained from the present LES simulations are compared with the Tollmien [3] and Görtler [4] theories in Fig. 6. The numerical results are expressed in function of the similarity variable, ζ , and are plotted at different axial coordinates, to show that the hypothesis of self-similarity is confirmed. The velocity profile in the PCR is a monotonic function of the vertical coordinate, having a maximum on the centerline and going to zero far away. Both theories give comparable results at the interface. Despite the fact that at higher Reynolds numbers the effect of the disturbances is stronger, the agreement between the present numerical results and the two theoretical values is quite good.

Figure 6. Axial velocity in PCR: numerical (points), Tollmien (black line) and Görtler theories (dashed line): (a) Re = 5000; (b) Re = 10,000; (c) Re = 20,000; (d) Re = 40,000.

The exam of the comparisons, carried out in sections 3.3 and 3.4, are important because they confirm that upstream the fully developed zone, two self-similar regions are present: the first one follows the behaviour introduced in [1] for a two-dimensional case, while the second one follows the well-known theories of Tollmien [3] and Görtler [4].

3.5 Self-similar solutions in the FDR.

Downstream the PCR is present the Fully Developed Region, FDR, which begins after the point where the turbulence has penetrated into the axis. After the PCR the mean axial velocity on the centerline, which remains constant from the slot exit, starts decreasing with the square root of the axial coordinate up to a point where is negligible.

The isotach curves in the FDR, derived from the three-dimensional numerical simulations, are reported in Fig. 7. The slope of the isotach curves in the FDR is always positive, meaning that no curve in the *x-y* plan has an axial velocity remaining constant, which is the characteristic of the FDR.

Figure 7. Numerical isotach curves in FDR. U/U_c = 0.3: numerical (black points) and regression (black line). U/U_c = 0.5: numerical (white point) and regression (dot-dashed line). U/U_c = 0.7: numerical (x point) and regression (point line). U/U_c = 0.9: numerical (diamond point) and regression (dashed line). (a) Re = 5000; (b) Re = 10,000; (c) Re = 20,000; (d) Re = 40,000.

The conservation of the axial and vertical momentum lead to the following equations

$$U\frac{\partial U}{\partial x}+V\frac{\partial U}{\partial y}=\frac{\partial}{\partial y}\left(\nu_T\frac{\partial U}{\partial y}\right) \tag{25}$$

$$0=-\frac{\partial P}{\partial y}+\frac{\partial \tau_{yy}^{R}}{\partial y} \tag{26}$$

The mean continuity equation is enforced by the use of the mean stream-function, Ψ , defined by

$$\Psi=U_c\cdot\sigma\cdot\left(x-L_s\right)\cdot f \tag{27}$$

being *f* a function of the self-similar variable chosen, and

$$U_c = \frac{n}{\sqrt{x - L_s}} \tag{28}$$

the axial velocity at the centerline.

The theories of Tollmien [3] and Görtler [4] differ in the definition of the turbulent viscosity, which is

$$\nu_T = c^2 \cdot \left(x - L_s\right)^2 \cdot \left|\frac{\partial U}{\partial y}\right| \tag{29}$$

in [3], and

$$\nu_T = g \cdot U_c \cdot \left(x - L_s\right) \tag{30}$$

in [4].

The problem is solved in [3] by using the following self-similar variable

$$\zeta = \frac{1}{\sqrt[3]{2c^2}} \frac{y}{\left(x - L_s\right)} \tag{31}$$

leading to the following ordinary differential equation

$$\frac{d}{d\zeta}\left(\left|\frac{d^2 f}{d\zeta^2}\right| \frac{d^2 f}{d\zeta^2} + f \frac{df}{d\zeta}\right) = 0 \tag{32}$$

while the self-similar variable is defined in [4] as

$$\xi = \frac{\sigma}{4g} \frac{y}{\left(x - L_s\right)} \tag{33}$$

leading to

$$\frac{d}{d\xi}\left(\frac{df}{d\xi} + f^2\right) = 0 \tag{34}$$

The two mean velocity components are defined as

$$U = U_c \frac{\sigma}{\sqrt[3]{2c^2}} \frac{df}{d\zeta} = U_c \frac{\sigma^2}{4g} \frac{df}{d\xi} \tag{35}$$

$$V = -U_c \cdot \sigma \cdot \left(\frac{1}{2} f(\zeta) - \zeta \frac{df}{d\zeta} \right) = -U_c \cdot \sigma \cdot \left(\frac{1}{2} f(\xi) - \xi \frac{df}{d\xi} \right) \quad (36)$$

The constant σ is function of the Reynolds number. Abramovich [49] has chosen values of σ that span between 0.09 and 0.12 giving $U/U_c = 0.5$ at $(\eta = 1)$, while, in the present work, σ spans between 0.06 and 0.1. Equations (32) and (34) are solved providing the boundary conditions imposed in [3] and [4].

The comparison between the mean axial velocity profiles, obtained with the present numerical approach, and the theoretical ones, [3] and [4], is shown in Fig. 8 at different Reynolds numbers. The velocity is scaled by its axial value and plotted versus *y/b*, where

$$b = \sigma_A (x - L_s) \quad (37)$$

and σ_A is the value of the constant σ such that $y/b(x) = 1 \Rightarrow U/U_c = 0.5$, [49].

Figure 8. Axial velocity in FDR: numerical (points), Tollmien (black line) and Görtler theories (dashed line): (a) Re = 5000; (b) Re = 10,000; (c) Re = 20,000; (d) Re = 40,000.

The agreement between the present numerical results and the theoretical ones is quite good. Both the theories of [3] and [4] give comparable results at the interface, where their solutions coincide. The present numerical results are in better agreement with [3] externally, while, in the center of the jet, the agreement is better with [4], the opposite of what happens for the PCR.

4. Conclusions

The aim of this work is to confirm the experiments of [14-20], that discovered the presence of a region of flow which can be considered "undisturbed" between the exit of the slot and the beginning of the PCR. This region, or type of flow, has been called Undisturbed Region of Flow, URF, in the average evolution, and Negligible Disturbance Flow, NDF, plus Small Disturbances Flow, SDF, in the instant evolution.

In order to confirm the experimental finding, three-dimensional numerical simulations are carried out at several Reynolds numbers by reproducing the boundary conditions of [2]. The present three-dimensional numerical simulations assume a top-hat velocity profile on the slot exit with a superimposed disturbance, which triggers the vortex stretching and consequently allows the FDR to appear as well. In the span-wise direction the "periodic" boundary condition has been used in order to have results independent on the slot width. The three-dimensional numerical results are validated against the theories of Tollmien [3] and Görtler [4] for both the Potential Core Region, PCR, and the Fully Developed Region, FDR, finding a good agreement.

The present results extend the results previously obtained in the two-dimensional analysis [1]. Despite the introduction of a disturbance on the velocity profile at the slot exit, the turbulent boundary layer does not form on the slot exit. A region of flow forms between the slot exit and the PCR, where the evolution of the

jet is driven by the viscous friction with the stagnant air. The length of this region of flow decreases with the increase of the Reynolds number and therefore, the theory of [2] still holds true at high Reynolds numbers, or for flows with strong perturbation added to the velocity profile at the slot exit.

Another important result is the conclusion that the velocity profile in the URF is self-similar, which holds true also in the three-dimensional case with the superimposed disturbance. The evolution of the jet depends on the boundary conditions on the slot exit and a different velocity profile may produce a different flow evolution. However, since the thickness of the shear layer is proportional to the distance from the slot exit, the top-hat velocity profile is the one for which the roller-vortices appear earlier, and therefore, it is the velocity profile which produces the shortest URF. In conclusion, a different velocity profile can make the URF longer, but not shorter. Another important factor which may affect the solution is the turbulence intensity at the slot exit. The 1% value superimposed on the velocity profile at the slot exit in the present simulations is plausible, but in other conditions the turbulence intensity can be higher.

The present three-dimensional numerical results, validated against the theories of [3] and [4], confirm more than a decade of experimental observations about the URF in the average flow, and the NDF and SDF in the instant flow, [14-20].

Acknowledgements

This project has been supported by CINECA/CASPUR with grant number std12-038.

References

[1] Andrea Boghi, Matteo Angelino, Fabio Gori, Numerical Evidence of an Undisturbed Region of Flow in Turbulent Rectangular Submerged Free Jet, *Numerical Heat Transfer*, in press, (2016).

[2] M.L. Albertson, Y.B. Dai, R.A. Jensen, and H. Rouse, Diffusion of Submerged Jets, *Trans. Am. Soc. Civ. Eng.*, 410 vol. *115*, no. 1, pp. 639–64, 1950.

[3] W. Tollmien, Calculation of Turbulent Expansion Processes, *Zeitschrift Für Angewandte Mathematik Und*
Mechanik, vol. *6*, no. 6, pp. 468–78, 1926.

[4] H. Gortler, Berechnung von Aufgaben Der Freien Turbulenz Auf Grund Eines Neuen Naherungsansatzes,
Zeitschrift Für Angewandte Mathematik Und Mechanik, vol. *22*, no. 5, pp. 244–254, 1942.

[5] E. Forthmann, Turbulent Jet Expansion, NACA-TM-789, 1936.

[6] D.R. Miller and E.W. Comings, Static Pressure Distribution in the Free Turbulent Jet, *J. Fluid Mech*., vol. *3*, no. 1, pp. 1–16, 1957.

[7] B.G. Van der Hegge Zijnen, Measurements of the Distribution of Heat and Matter in a Plane Turbulent Jet of Air, *Appl. Sci. Res*., vol. *7*, no. 4, pp. 277–292, 1958.

[8] H.W. Liepmann and J.Laufer, Investigations of Free Turbulent Mixing, *NACA Technical Note*, 1947.

[9] F.O. Thomas and V.W. Goldschmidt, Structural Characteristics of a Developing Turbulent Planar Jet, *J. Fluid Mech*., vol. *163*, pp. 227–256, 1986.

[10] L.J.S. Bradbury, The Structure of a Self-Preserving Turbulent Plane Jet, *Journal of Fluid Mechanics* 23, no. 01 (1965): 31–64.

[11] E. Gutmark, and I. Wygnanski, The Planar Turbulent Jet, *Journal of Fluid Mechanics* 73, no. 3 (1976): 465.

[12] A.A. Sfeir, The Velocity and Temperature Fields of Rectangular Jets, *International Journal of Heat and Mass Transfer* 19, no. 11 (November 1976): 1289–97.

[13] A. Krothapalli, D. Baganoff, and K. Karamcheti, On the Mixing of a Rectangular Jet, *Journal of Fluid Mechanics* 107 (1981): 201–20.

[14] F. Gori, F. De Nigris, and E. Nino, Fluid Dynamics Measurements and Optical Visualization of the Evolution of a Submerged Slot Jet of Air, *The 12th International Heat Transfer Conference, Grenoble, France*, vol. *2*, pp. 303–308, 2002.

[15] F. Gori and I. Petracci, Fluid Dynamics Measurements and Numerical Simulations around a Circular Cylinder Impinged by a Submerged Slot Jet of Air, *American Society of Mechanical Engineers, Fluids Engineering Division* 440 *(Publication) FED*, vol. *259*, pp. 179–185, 2003.

[16] F. Gori, and I. Petracci, Fluid Dynamics Measurements in a Submerged Free Slot Jet of Air, *14th International Symposium on Transport Phenomena*, Bali, Indonesia, 6–10th July, pp. 491–496, 2003.

[17] F. Gori and E. Nino, Fluid Dynamics Measurements and Flow Visualizations of a Free Slot Jet of Air, *American Society of Mechanical Engineers*. Fluids Engineering Division (Publication), FED, vol. *259*, pp. 187–192, 2003.

[18] F. Gori, E. Nino, and I. Petracci, Shadowgraph Visualizations of a Submerged Free Slot Jet of Air, *Int. J. Heat Technol*., vol. *25*, no. 1, pp. 157–164, 2007.

[19] F. Gori, I. Petracci, and M. Angelino, Flow Evolution of a Turbulent Submerged Two-Dimensional Rectangular Free Jet of Air. Average Particle Image Velocimetry (PIV) Visualizations and Measurements, *Int. J. Heat Fluid Flow*, vol. *44*, pp. 764–775, 2013.

[20] F. Gori, I. Petracci, and M. Angelino, Influence of the Reynolds Number on the Instant Flow Evolution of a Turbulent Rectangular Free Jet of Air, *Int. J. Heat Fluid Flow*, vol. *50*, pp. 386–401, 2014.

[21] G.B. Brown, On Vortex Motion in Gaseous Jets and the Origin of Their Sensitivity to Sound, *Proc. Phys. Soc*., vol. *47*, p. 703, 1935.

[22] G.S. Beavers and T.A. Wilson, Vortex Growth in Jets, *J. Fluid Mech*., vol. *44*, pp. 97–112, 1970.

[23] A. Chambers, R. Antonia, L. Browne, Effect of Symmetry and Asymmetry of Turbulent Structures on the

Interaction Region of a Plane Jet, *Exp. Fluids*, vol. *3*, pp. 343–348, 1985.

[24] D.O. Rockwell, W.O. Niccolls, Natural Breakdown of Planar Jets, *J. Fluids Eng.* 94 (4), 720-728.

[25] S. Gogineni, C. Shih, Experimental investigation of the unsteady structure of a transitional plane wall jet, *Experiments in Fluids*, vol. 23, Is. 2, pp. 121-129 (1997)

[26] M.H. Yu, T.K. Lin, Y.Y. Hsieh, Influence of acoustic forcing on the near field development of a heated plane jet, *Experimental Thermal and Fluid Science*, vol. 25, Is. 1-2, pp. 13-22, (2001).

[27] F.B. Hsiao, Y.C. Lim, J.M. Huang, On the near-field flow structure and mode behaviors for the right-angle and sharp-edged orifice plane jet, *Experimental Thermal and Fluid Science*, vol. 34, Is. 8, pp. 1282-1289, (2010).

[28] S. Yuu, K. Ikeda, T. Umekage, Flow-field prediction and experimental verification of low Reynolds number gas-particle turbulent jets, *Colloids and Surfaces A: Physicochemical and Engineering Aspects* 109 (1996) 13-27.

[29] B. Rembold, N.A. Adams, and L. Kleiser, Direct Numerical Simulation of a Transitional Rectangular Jet, *International Journal of Heat and Fluid Flow* 23, no. 5 (October 2002): 547–53.

[30] Y. Liu, P.G. Tucker, R.M. Kerr, Linear and nonlinear model large-eddy simulations of a plane jet, *Computers & Fluids*, vol. 37, Is. 4, May 2008, pp. 439–449.

[31] F. Gori, M. Angelino, A. Boghi, and I. Petracci, Preliminary Numerical Solutions of the Evolution of Free

Jets, *ASME International Mechanical Engineering Conference and Exposition, Proceedings (IMECE),* vol. *7* (D), pp. 463–469, 2012.

[32] F. Gori and L. Bossi, On the Cooling Effect of an Air Jet along the Surface of a Cylinder, *International Communications in Heat and Mass Transfer*, Vol. 27, N. 5, pp. 667-676, 2000.

[33] F. Gori and L. Bossi, Optimal Slot Height in the Jet Cooling of a Circular Cylinder, *Applied Thermal Engineering*, 23 (7) pp. 859-870, May 2003.

[34] F. Gori, I. Petracci, Heat Transfer Measurements and Numerical Simulations in the Cooling of a Circular Cylinder by a Slot Jet of Air, *American Society of Mechanical Engineers*, Heat Transfer Division, (Publication) HTD, 374, 1 (2003): 3-9.

[35] B. Srinivasan, A. Dewan, LES of a Turbulent Slot Impinging Jet to Predict Fluid Flow and Heat Transfer, *Numerical Heat Transfer, Part A: Applications*, 64, 10 (2013): 759-776.

[36] F. Gori, P. Coppa, Circumferential variation of heat transfer on three circular cylinders cooled by a slot jet of air, *International Journal of Heat and Technology*, 16, 2 (1998): 63-69.

[37] F. Gori, I Petracci, V. Tedesco, Cooling of two smooth cylinders in row by a slot jet of air with low turbulence, *Applied Thermal Engineering*, 27, 14-15 (2007) : 2415-2425.

[38] F. Gori, F. De Nigris, E. Pippione and G. Scavarda, Cooling of Finned Cylinders by a Jet Flow of Air, *American Society of Mechanical Engineers*, Process Industries Division (Publication), PID, 7 (2002) 117-122.

[39] F. Gori, M. Borgia and A. Doro Altan, Cooling of a Finned Cylinder by a Jet Flow of Air, *American Society of Mechanical Engineers,* Process Industries Division (Publication) PID, 8 (2003) 147-152.

[40] F. Gori, M. Borgia, A. Doro Altan, M. Mascia and I. Petracci, Cooling of a Finned Cylinder by a Jet Flow of Air, *ASME Journal of Heat Transfer*, 127 (12) pp.1416-1421, December 2005.

[41] F. Gori, M. Mascia, I. Petracci, Air cooling of a finned cylinder with slot jets of different height, *International Journal of Thermal Sciences*, 50 (2011): 1583-1593.

[42] Ivano Petracci, Luca Manni, Fabio Gori, Numerical simulation of the optimal spacing for a radial finned tube cooled by a rectangular jet. I-Average thermal results, *International Journal of Thermal Sciences*, 104 (2016) 54-67.

[43] F. Gori, I. Petracci, Influence of turbulence on heat transfer upon a cylinder impinged by a slot jet of air, *Applied Thermal Engineering*, 49, (2012): 106-117.

[44] Fabio Gori, Ivano Petracci, Influence of screen solidity ratio on heat transfer upon a cylinder impinged by a rectangular jet, *International Journal of Heat and Mass Transfer*, 81 (2015) 19-27.

[45] F. Gori, I. Petracci, On the Effect of the Slot Height in the Cooling of a Circular Cylinder with a Rectangular Jet, *International Communications in Heat and Mass Transfer*, 48 (2013): 8-14.

[46] F. Gori, I. Petracci, M. Angelino, Experimental and Numerical Heat Transfer on a Cylinder Cooled by Two Rectangular Jets of Different Heights, *ASME International Mechanical Engineering Conference and Exposition, Proceedings (IMECE), Houston, Texas, USA*, 7 (D), (2012): 2679-2688.

[47] S. Lee, S. Lele, P. Moin, Simulation of spatially evolving compressible turbulence and the application of taylors hypothesis, *Phys. Fluids*, A 4 (1992) 1521–1530.

[48] S. Chandrasekhar, *Hydrodynamic and Hydromagnetic Stability*, Clarendon Press: Oxford University Press, 1961.

[49] G.N. Abramovich, *The Theory of Turbulent Jets*, English Translation published by M.I.T. Press, Massachusetts, 1963.

Captions to figures.

Figure 1. Instant vorticity iso-surfaces colored by instant velocity magnitude: (a) Re = 5000; (b) Re = 10,000; (c) Re = 20,000; (d) Re = 40,000.

Figure 2. Instant isobaric surfaces and velocity vectors: (a) Re = 5000; (b) Re = 10,000; (c) Re = 20,000; (d) Re = 40,000.

Figure 3. Turbulent kinetic energy contours: (a) Re = 5000; (b) Re = 10,000; (c) Re = 20,000; (d) Re = 40,000.

Figure 4. $\overline{u'v'}$ *contours: (a) Re = 5000; (b) Re = 10,000; (c) Re = 20,000; (d) Re = 40,000.*

Figure 5. Axial velocity in URF: numerical (points) and present theory of self-similarity (black line): (a) Re = 5000; (b) Re = 10,000; (c) Re = 20,000; (d) Re = 40,000.

Figure 6. Axial velocity in PCR: numerical (points), Tollmien (black line) and Görtler theories (dashed line): (a) Re = 5000; (b) Re = 10,000; (c) Re = 20,000; (d) Re = 40,000.

Figure 7. Numerical isotach curves in FDR. U/U_c *= 0.3: numerical (black points) and regression (black line).* U/U_c *= 0.5: numerical (white point) and regression (dot-dashed line).* U/U_c *= 0.7: numerical (x point) and regression (point line).* U/U_c *= 0.9: numerical (diamond point) and regression (dashed line). (a) Re = 5000; (b) Re = 10,000; (c) Re = 20,000; (d) Re = 40,000.*

Figure 8. Axial velocity in FDR: numerical (points), Tollmien (black line) and Görtler theories (dashed line): (a) Re = 5000; (b) Re = 10,000; (c) Re = 20,000; (d) Re = 40,000.

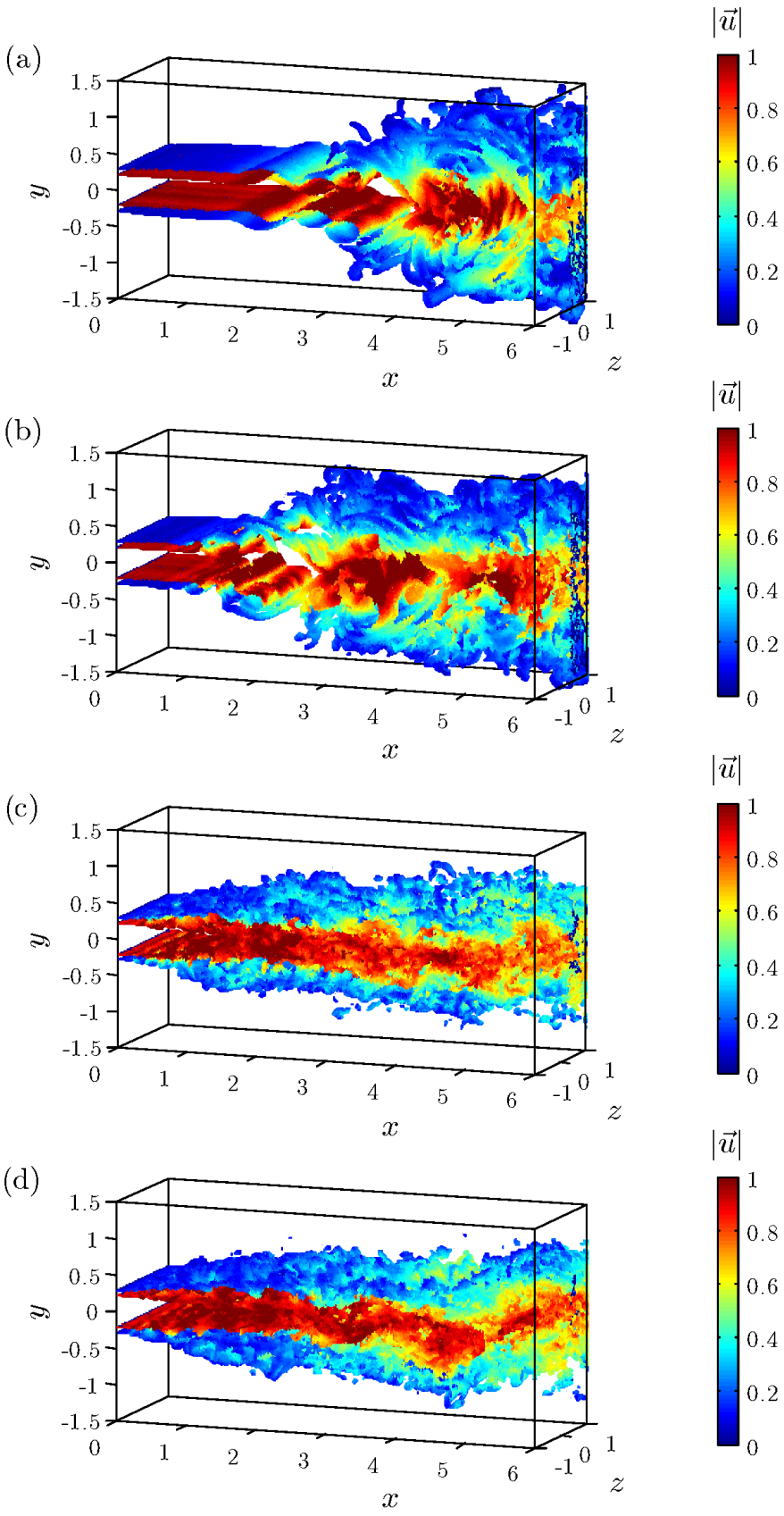


Figure 1. Instant vorticity iso-surfaces colored by instant velocity magnitude: (a) Re = 5000; (b) Re = 10,000; (c) Re = 20,000; (d) Re = 40,000.

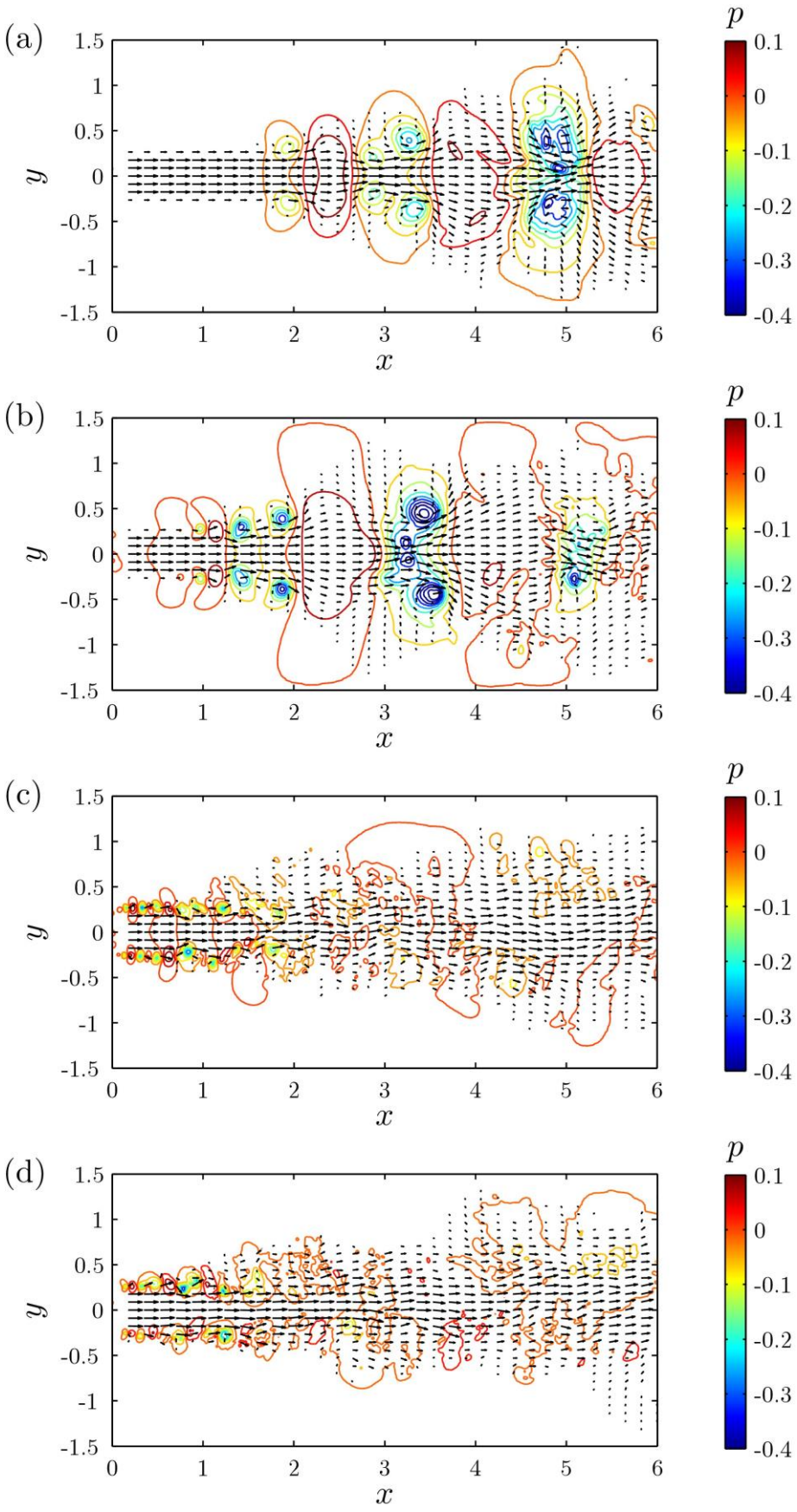


Figure 2. Instant isobaric surfaces and velocity vectors: (a) Re = 5000; (b) Re = 10,000; (c) Re = 20,000; (d) Re = 40,000.

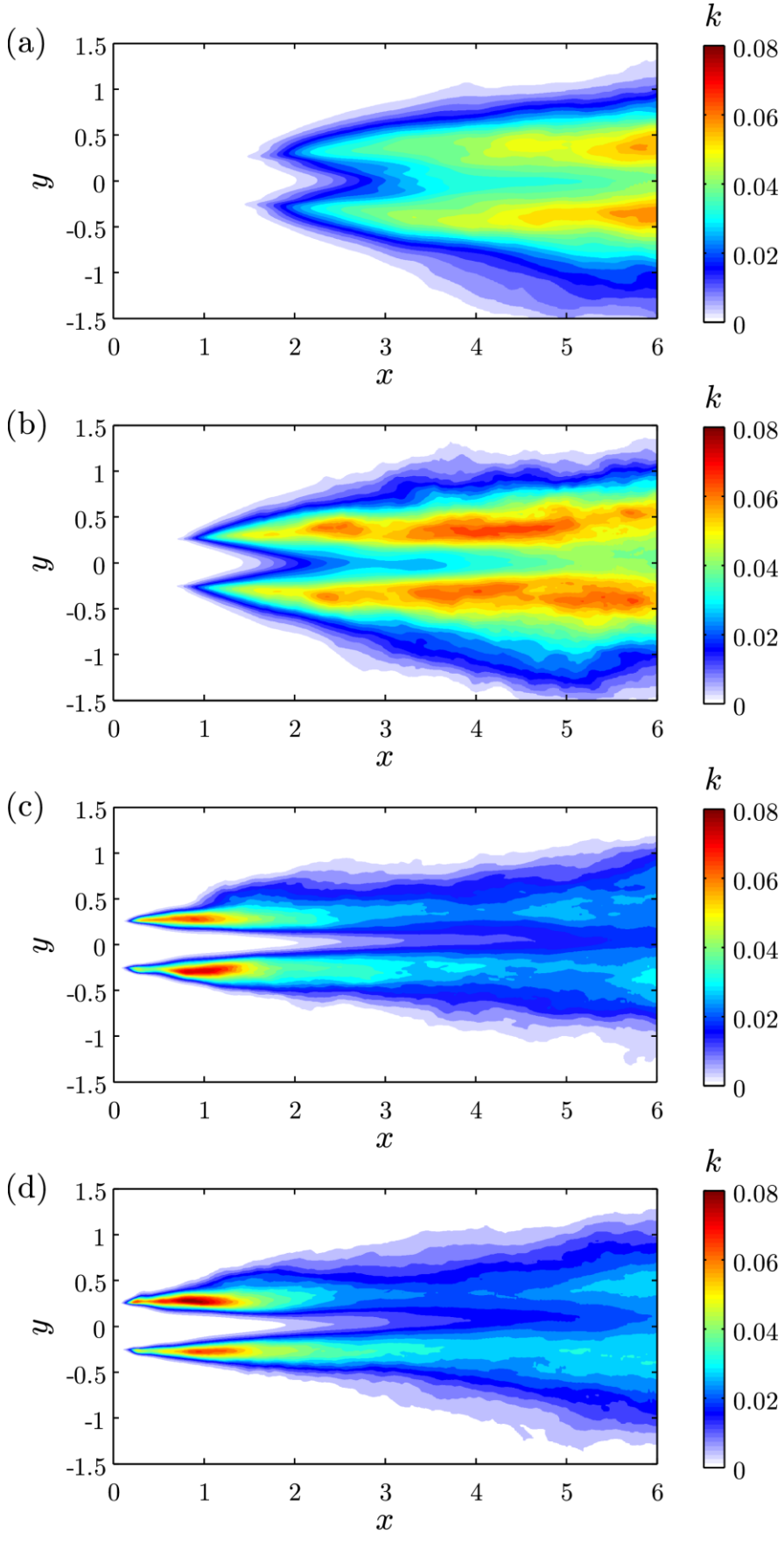

(a)
(b)
(c)
(d)
k
0.08
0.06
0.04
0.02
0
y
x
1.5
1
0.5
0
-0.5
-1
-1.5
0
1
2
3
4
5
6

Figure 3. Turbulent kinetic energy contours: (a) Re = 5000; (b) Re = 10,000; (c) Re = 20,000; (d) Re = 40,000.

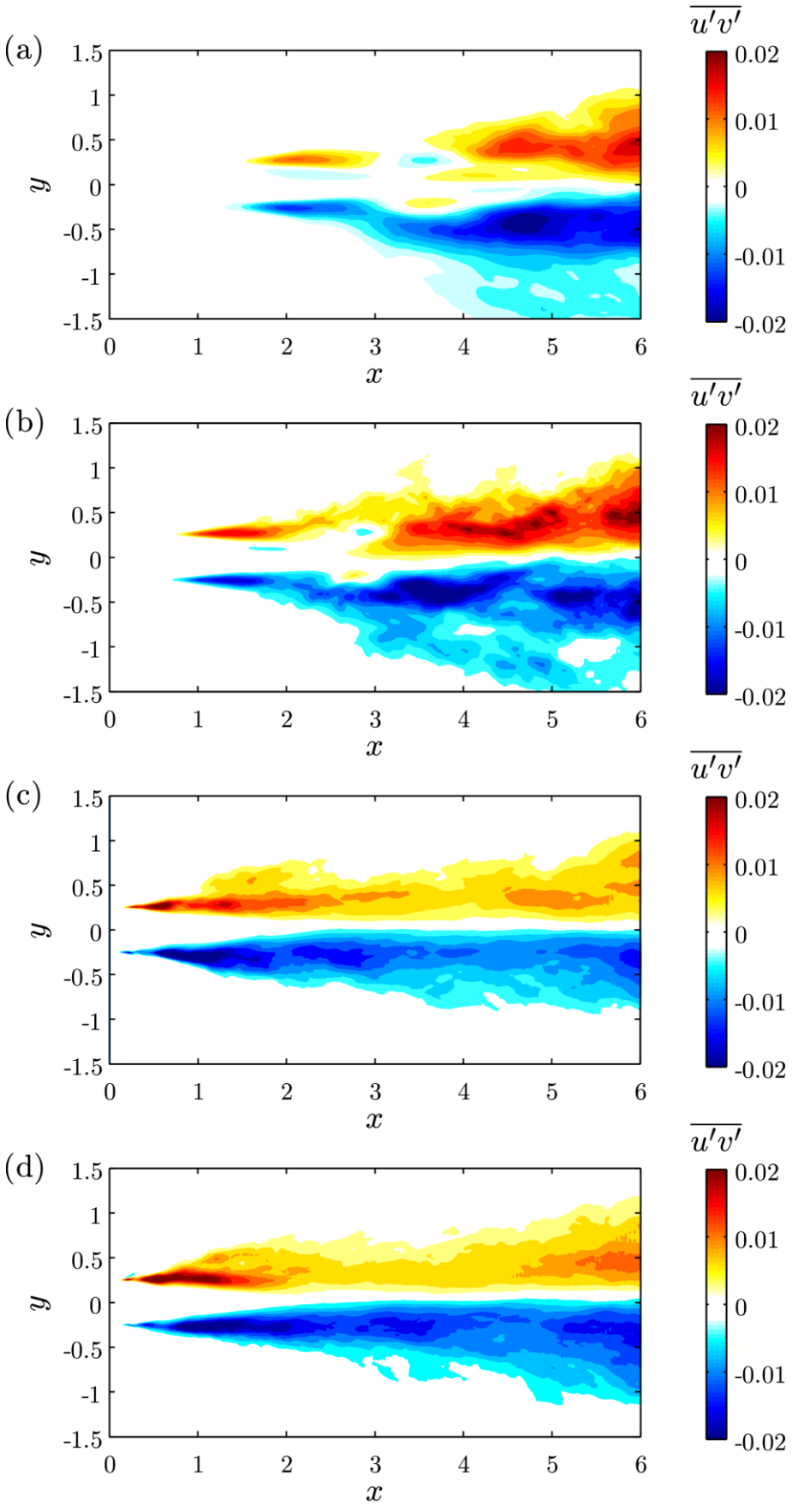


Figure 4. $\overline{u'v'}$ *contours: (a) Re = 5000; (b) Re = 10,000; (c) Re = 20,000; (d) Re = 40,000.*

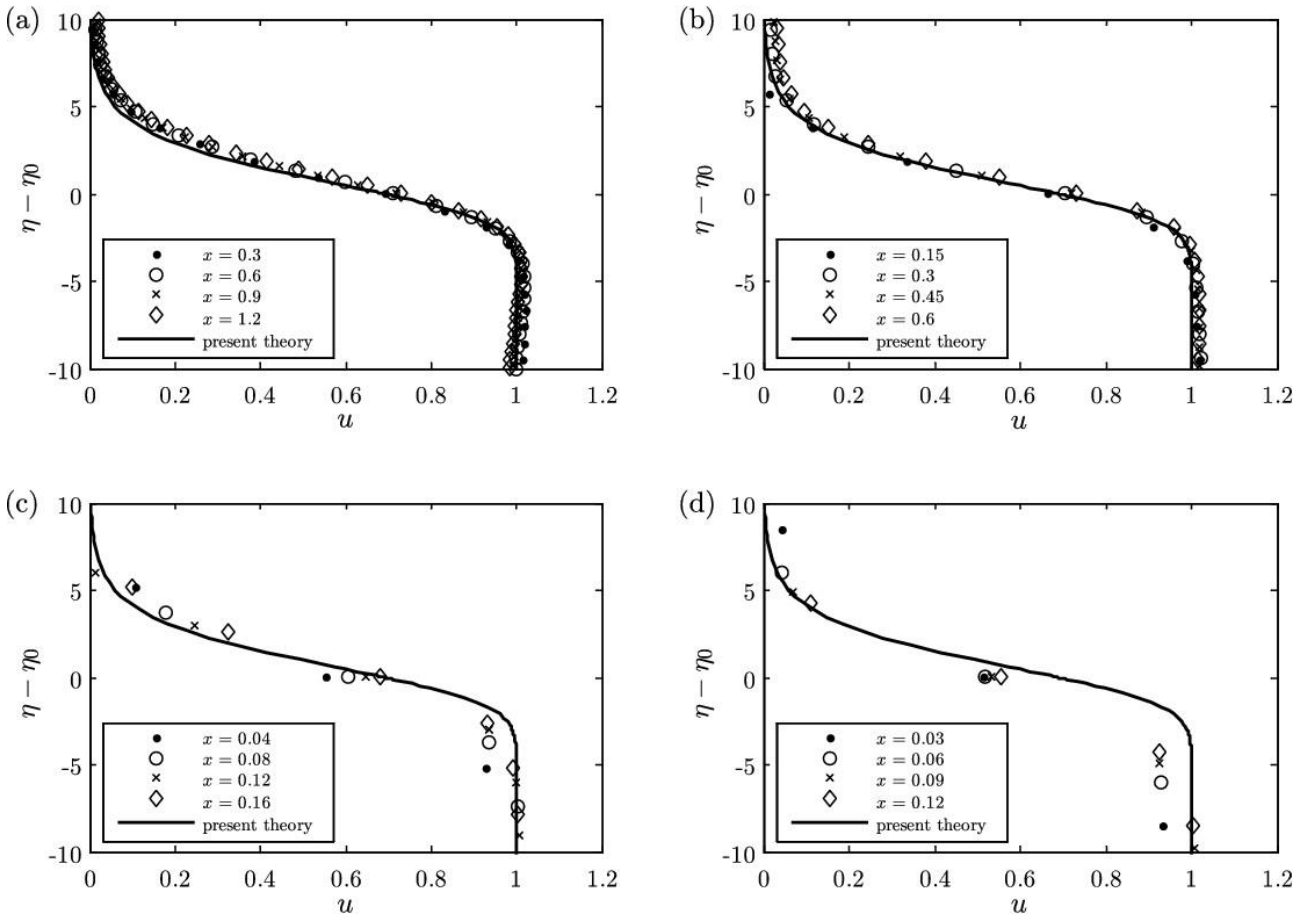


Figure 5. Axial velocity in URF: numerical (points) and present theory of self-similarity (black line): (a) Re = 5000; (b) Re = 10,000; (c) Re = 20,000; (d) Re = 40,000.

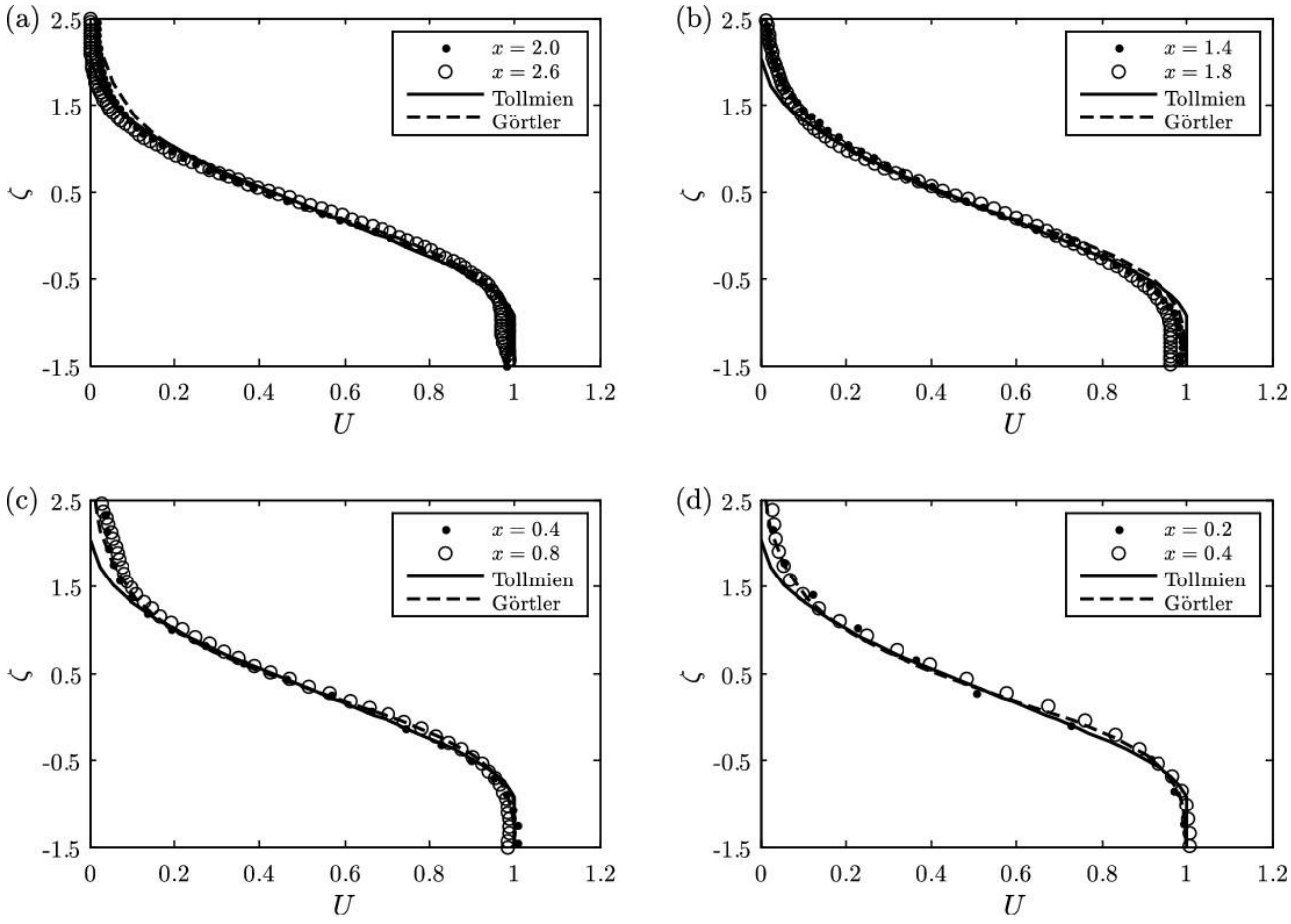


Figure 6. Axial velocity in PCR: numerical (points), Tollmien (black line) and Görtler theories (dashed line): (a) Re = 5000; (b) Re = 10,000; (c) Re = 20,000; (d) Re = 40,000.

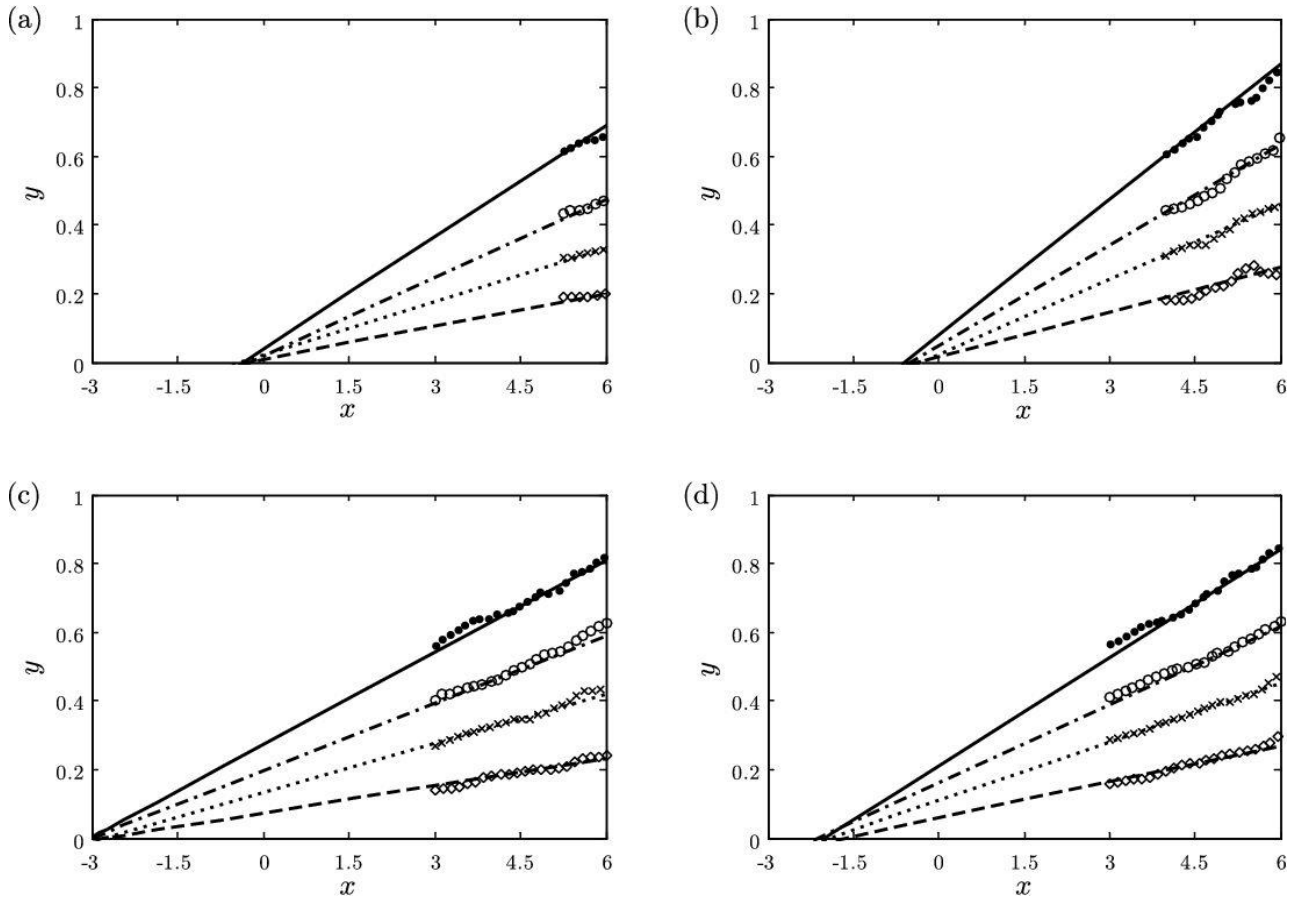


Figure 7. Numerical isotach curves in FDR. U/U_c = 0.3: numerical (black points) and regression (black line). U/U_c = 0.5: numerical (white point) and regression (dot-dashed line). U/U_c = 0.7: numerical (x point) and regression (point line). U/U_c = 0.9: numerical (diamond point) and regression (dashed line). (a) Re = 5000; (b) Re = 10,000; (c) Re = 20,000; (d) Re = 40,000.

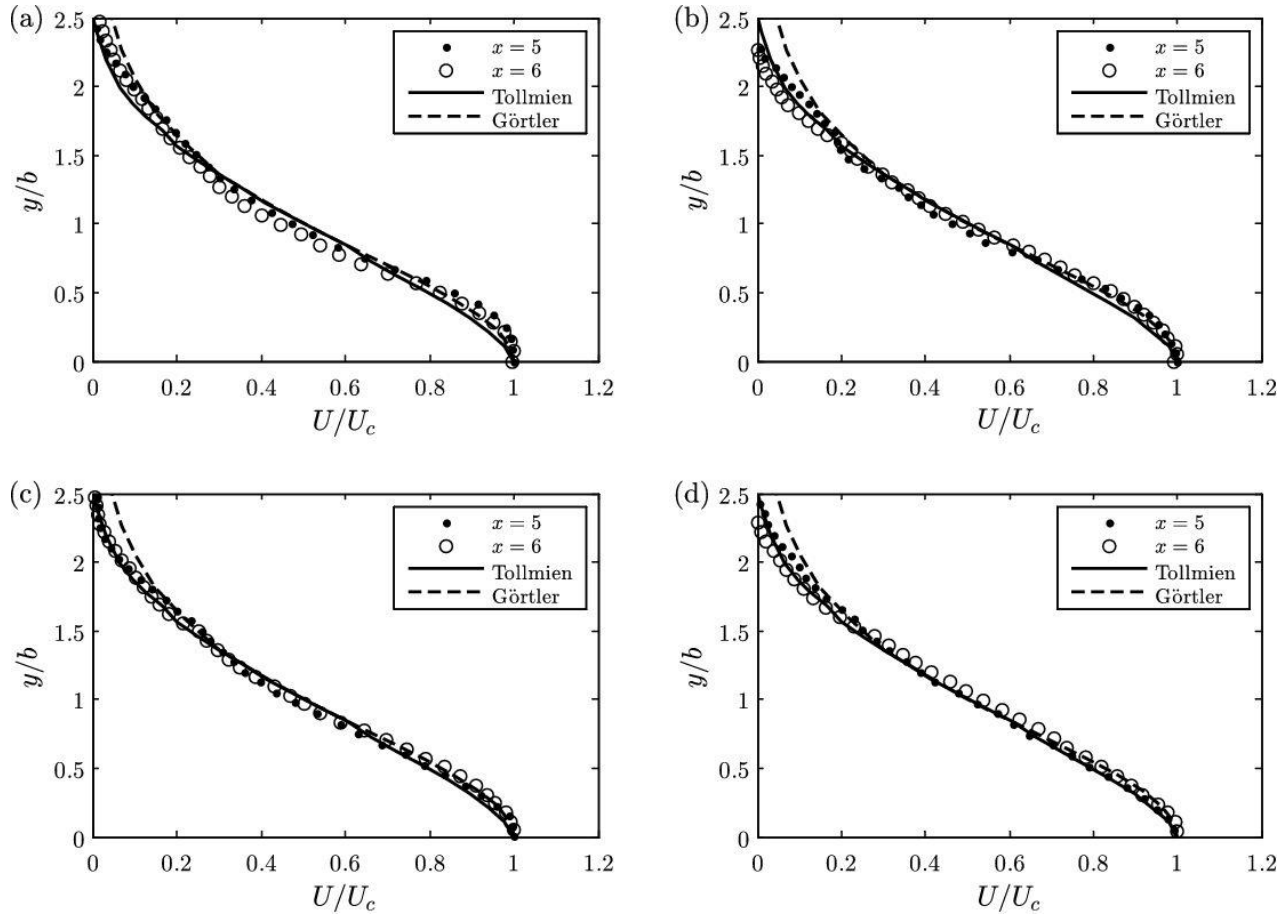


Figure 8. Axial velocity in FDR: numerical (points), Tollmien (black line) and Görtler theories (dashed line): (a) Re = 5000; (b) Re = 10,000; (c) Re = 20,000; (d) Re = 40,000.



https://dspace.org/

Numerical solution of three-dimensional rectangular submerged jets with evidence of the undisturbed region of flow

Angelino, M.; Boghi, Andrea; Gori, Fabio

2016-09-20
Taylor & Francis
http://dx.doi.org/10.1080/10407782.2016.1214494
Angelino, M., Boghi, A., Gori, F. (2016) Numerical solution of three-dimensional rectangular submerged jets with evidence of the undisturbed region of flow, Numerical Heat Transfer, Part A: Applications, volume 70, Issue 8, pages 815-830

Downloaded from a DSpace repository. https://dspace.org/